nanomaterials

MDPI

Article

Fabrication of Hierarchical MOF-Derived $NiCo_2S_4$@Mo-Doped Co-LDH Arrays for High-Energy-Density Asymmetric Supercapacitors

Siyi Cheng, Kang Du, Xiaowu Wang, Yufei Han, Longxiao Li and Guojun Wen *

School of Mechanical Engineering and Electronic Information, China University of Geosciences, Wuhan 430074, China; chengsiyi@cug.edu.cn (S.C.)
* Correspondence: wenguojun@cug.edu.cn; Tel.: +86-27-67883421

Abstract: The rational fabrication of composite structures made of mixed components has shown great potential for boosting the energy density of supercapacitors. Herein, an elaborate hierarchical MOF-derived $NiCo_2S_4$@Mo-doped Co-LDH arrays hybrid electrode was fabricated through a stepwise method. By leveraging the synergistic effects of a uniform array of $NiCo_2S_4$ nanowires as the core and an MOF-derived porous shell, the $NiCo_2S_4$@Mo-doped Co-LDH hybrid electrode demonstrates an exceptional specific capacitance of 3049.3 F g^{-1} at 1 A g^{-1}. Even at a higher current density of 20 A g^{-1}, the capacitance remains high at 2458.8 F g^{-1}. Moreover, the electrode exhibits remarkable cycling stability, with 91% of the initial capacitance maintained after 10,000 cycles at 10 A g^{-1}. Additionally, the as-fabricated asymmetric supercapacitor (ASC) based on the $NiCo_2S_4$@Mo-doped Co-LDH electrode achieves an impressive energy density of 97.5 Wh kg^{-1} at a power density of 835.6 W kg^{-1}. These findings provide a promising approach for the development of hybrid-structured electrodes, enabling the realization of high-energy-density asymmetric supercapacitors.

Keywords: asymmetric supercapacitors; $NiCo_2S_4$; Co-LDH; cross-linked; Mo-doped; high energy density

check for updates

Citation: Cheng, S.; Du, K.; Wang, X.; Han, Y.; Li, L.; Wen, G. Fabrication of Hierarchical MOF-Derived $NiCo_2S_4$@Mo-Doped Co-LDH Arrays for High-Energy-Density Asymmetric Supercapacitors. *Nanomaterials* **2023**, *13*, 2663. https://doi.org/10.3390/nano13192663

Academic Editors: Fabrizio Pirri and Diego Cazorla-Amorós

Received: 4 September 2023
Revised: 23 September 2023
Accepted: 27 September 2023
Published: 28 September 2023

Correction Statement: This article has been republished with a minor change. The change does not affect the scientific content of the article and further details are available within the backmatter of the website version of this article.

Copyright: © 2023 by the authors. Licensee MDPI, Basel, Switzerland. This article is an open access article distributed under the terms and conditions of the Creative Commons Attribution (CC BY) license (https://creativecommons.org/licenses/by/4.0/).

1. Introduction

Highly efficient energy storage systems are essential for reducing environmental pollution, geothermal problems, and energy shortage. Among them, supercapacitors have drawn abundant attention due to their exceptional cycle stability, high power density, and fast charge/discharge capabilities [1–3]. However, relatively lower energy density than secondary battery systems has restricted their potential for long-term applications [4,5]. The energy density of supercapacitors has been improved by fabricating asymmetric supercapacitors with large voltage windows, as well as developing high-capacitive electrode materials according to $E = \frac{1}{2}CV^2$ [6,7]. Asymmetric supercapacitors have emerged as a promising solution to bridge the gap between electrical double-layer capacitors (EDLCs) and pseudocapacitors, which are classified based on their charge storage mechanisms. To achieve this, researchers have explored different strategies to integrate materials from both types, aiming to enhance the performance and energy storage capabilities of these devices [8–10].

High-specific-capacitance pseudocapacitive material, as an essential part of asymmetric supercapacitors, is crucial for increasing energy density [11]. Recently, pseudocapacitive materials based on hierarchical core-shell structures have been extensively studied due to the adjustable heterostructures, rich redox sites, sufficient electrode/electrolyte contact area, and efficient ion transportation path [12–15]. Among different materials, $NiCo_2S_4$ is promising for use in supercapacitors because its rich electrochemistry can be easily activated by means to improve the specific capacitance, ion diffusion kinetics, and cyclability. These strategies, particularly those combining $NiCo_2S_4$ with trimetallic oxides and layered double oxides (LDHs) that lead to highly porous core-shell architecture, have

demonstrated outstanding performance [16–20]. In our previous work, using $NiCo_2S_4$ as scaffold to construct core-shell structures has been proven effective at increasing the energy density of asymmetric supercapacitors [21,22]. Hence, exploring new strategies for fabricating a $NiCo_2S_4$-based core-shell structure to further enhance supercapacitor performance is promising.

Hydrotalcite-like ionic layered structures, adjustable chemical composition, and high redox activity make layered double hydroxides (LDHs) attractive as electrode materials in supercapacitors [23–25]. By integrating LDHs on $NiCo_2S_4$, the high-conductivity core facilitates the electron/ion transport. In contrast, the utilization of a shell with a significantly large specific surface area facilitates efficient ion transport and accelerates the transfer of electrons and ions. In this way, electrochemical performance can be much improved. Among different LDH synthesis methods, using metal organic frameworks (MOFs) as template could improve specific surface areas, facilitate electron transport, and increase the number of electroactive sites, leading to a higher specific capacitance and robust cycle stability [26–29]. Due to its clearly delineated structure and composition, endowed with traits conducive to viability, the incorporation of secondary metals in the electrode material holds significant potential for achieving the desired properties, opening up new possibilities for future applications. Furthermore, the persistent affinity of substrate molecules towards unsaturated sites, even after the post-treatment process, combined with the presence of extensive cavities, not only enhances reaction kinetics but also preserves rate efficiency [30,31].

Herein, a rational MOF-derived $NiCo_2S_4$@Mo-doped Co-LDH core-shell structure was fabricated through a step-wise method. In particular, $NiCo_2S_4$ nanowires, as the core material, are not only highly pseudocapacitive but also provide conductive support for Mo-doped Co-LDH. The implementation of a core-shell structure significantly enhances the nanomaterial's specific surface area, and provides protection for $NiCo_2S_4$ during the cycling process. Due to the synergistic effect, this unique structure of $NiCo_2S_4$@Mo-doped Co-LDH delivers extraordinary electrochemical performance. The asymmetric supercapacitor (ASC) device also performed exceptionally well. The remarkable electrochemical properties exhibited by the core-shell $NiCo_2S_4$@Mo-doped Co-LDH, synthesized using MOF as a template, present a promising approach for the development of high-energy-density supercapacitors.

2. Materials and Methods

2.1. Synthesis of $NiCo_2S_4$ Nanowires

Initially, a carbon cloth measuring 3×4 cm^2 was prepared and subjected to sequential cleaning in acetone, ethanol, and distilled water for a duration of 30 min using ultrasonic treatment. The synthesis of $NiCo_2S_4$ involved the following steps: Urea (0.726 g), $CoCl_2 \cdot 6H_2O$ (1.954 g), and $NiCl_2 \cdot 6H_2O$ (0.951 g) were dissolved in 60 mL of deionized water and stirred magnetically for 1 h. The carbon cloth was then submerged in the solution mentioned earlier and introduced into an autoclave, where it was subjected to a thermal treatment at 120 °C for 6 h. Subsequently, the cloth was allowed to cool naturally. In the final step, the carbon cloth, now loaded with the precursor, was immersed in a 70 mL aqueous solution of $Na_2S_9 \cdot H_2O$ (4.8 g) and held at a temperature of 160 °C for a duration of 6 h.

2.2. Synthesis of $NiCo_2S_4$@Co-MOF

To synthesize $NiCo_2S_4$@Co-MOF, A ($Co(NO_3)_2 \cdot 6H_2O$ (0.727 g) in 50 mL of DI water) and B (2-methylimidazole (2-MIM) (1.642 g) in 50 mL of DI water) were prepared in advance. Then, solution B was rapidly added to solution A, and the resulting mixture was vigorously stirred. Following this, the $NiCo_2S_4$ sample was immersed in the mixed solution and allowed to age for 4 h at room temperature. The color of the sample transitioned from black to purple during the aging process. The sample was then washed with methanol and subsequently dried at 60 °C for 12 h to obtain $NiCo_2S_4$@Co-MOF.

2.3. Synthesis of $NiCo_2S_4$@ Mo-Doped Co-LDH

In a typical synthesis procedure, a mixture of 20 mL ethanol and 40 mL deionized water was prepared, and 0.3 g of $Na_2MoO_4 \cdot 2H_2O$ was dissolved in this solution with continuous stirring to achieve homogeneity. Subsequently, the synthesized $NiCo_2S_4$@Co-MOF sample was immersed in this solution and subjected to treatment at 80 °C for 3 h. After cooling, the sample was washed with ethanol and subsequently dried at 60 °C overnight to obtain a hierarchical core-shell nanostructure of $NiCo_2S_4$@Mo-doped Co-LDH.

2.4. Material Characterizations

The synthesized samples underwent characterization to determine their phase, morphology, and microstructure. Phase analysis was conducted using a Bruker X-ray diffractometer (XRD), while morphological examination was performed using a NovaNano-450 FEI field emission scanning electron microscope (FESEM). Microstructural analysis was carried out using a JEM-2100 transmission electron microscope (TEM). Additionally, the surface characteristics of the samples were investigated using X-ray photoelectron spectroscopy (XPS) with an Escalab250 instrument.

2.5. Electrochemical Measurements

Various techniques were employed to evaluate the electrochemical performance of the electrodes prepared in this study. The electrochemical workstation (PARSTAT-3000A-DX) was utilized to conduct cyclic voltammetry (CV), galvanostatic charge–discharge (GCD), and electrochemical impedance spectroscopy (EIS) in a 3 M KOH electrolyte. To assess the cyclic stability of the electrodes, a battery test system (LAND CT3002A) was employed. In the three-electrode configuration, the working electrode consisted of the prepared samples, the reference electrode was Hg/HgO, and the counter electrode was composed of a Pt plate. The frequency range for EIS measurements spanned from 100 kHz to 0.01 Hz. The electrode capacitance can be determined by analyzing the GCD curve using the following equation:

$$C_s = I\Delta t / m\Delta V \tag{1}$$

where C_s represents the specific capacitance (F g^{-1}), I stands for the discharge current (A), t is the discharge time (s), V is the discharge voltage (V), and m is the mass of the active material (g).

2.6. Preparation of All-Solid-State Asymmetric Supercapacitor (ASC)

Utilizing the $NiCo_2S_4$@Mo-doped Co-LDH as the positive electrode and activated carbon (AC) as the negative electrode, an ASC device was constructed. Achieving optimal performance necessitates ensuring charge balance between the two electrodes:

$$\frac{m_+}{m_-} = \frac{C_{S-}\Delta V_-}{C_{S+}\Delta V_+} \tag{2}$$

where m stands for the mass of active material (g), C_S is the specific capacitance (F g^{-1}), and V is the voltage range (V). The specific capacitance of the electrodes could be calculated by the GCD results.

To construct an asymmetric supercapacitor (ASC), the electrodes and filter paper were immersed separately in a PVA-KOH solution for a duration of 15 min. Following this, they were assembled in a sandwich configuration. The electrochemical performance of the ASC device was evaluated by determining the energy density (E, Wh kg^{-1}) and power density (W kg^{-1}) through the utilization of the following equations:

$$E = C(\Delta U)^2 / 7.2 \tag{3}$$

$$P = 3600E / \Delta t \tag{4}$$

3. Results and Discussion

3.1. Preparation and Characterizations of the $NiCo_2S_4$@Mo-Doped Co-LDH

Figure 1a exhibits the synthesis process of the $NiCo_2S_4$@Mo-doped Co-LDH. $NiCo_2S_4$ nanowires were fabricated by a conventional hydrothermal method, which was reported in our previous work. With the initial hydrothermal treatments, the carbon fibers were evenly coated by the NiCo-precursor nanowires (Figure S1). During this process, the NiCo-precursor nanowires were directly grown on carbon by the reaction containing Ni^{2+}, Co^{2+}, and urea. Urea was used as the surfactant for the assemble of nanowire structures [32]. The surfaces of the NiCo-precursor nanowires are smooth, and the average diameter is about 240 nm. After the sulfuration process, the as-synthesized $NiCo_2S_4$ nanowires were uniformly anchored on carbon fibers (Figure 1b,c), which act as a good scaffold for MOF. Subsequently, with a chemical bath treatment in $Co(NO_3)_2$/2-MIM mixed solution, well-defined ZIF-67 nanosheets (polyhedrons) are coated on the $NiCo_2S_4$ nanowires to form $NiCo_2S_4$@ZIF-67 core-shell structures (Figure 1d,e). Finally, with Na_2MoO_4 in ethanol/DI water as etching solution, Mo ions could be immersed into ZIF-67 to release Co^{2+}. Co^{2+}/Co^{3+} and Mo ions combine with hydroxide ions to generate Mo-doped Co-LDH. The ZIF-67 template was converted into Mo-doped Co-LDH after 3 h of reaction, but the nanosheet profile and the solid bonding with $NiCo_2S_4$ nanowires are left unaltered (Figure 1f,g). Various synthesis timeframes were used to create samples in order to analyze the synthesis mechanism of Mo-doped Co-LDH structures. During brief reaction periods (2 h), the surfaces of $NiCo_2S_4$@Mo-doped Co-LDH exhibited a subtle increase in roughness in comparison to ZIF-67. Notably, no nanoflakes were observed atop the nanosheets, suggesting that the etching process remains incomplete. (Figure S1a,b). With the extension of the synthesis duration to 3 h, the ZIF-67 template remained remarkably unaltered, while the Mo-doped Co-LDH evolved into exquisite 2D nanoflakes, exhibiting elegant growth patterns (Figure S2b,e). The hierarchical arrangement bestowed an expansive active surface, thereby augmenting the capacitance. However, upon prolonging the reaction time to 4 h, the Mo-doped Co-LDH continues its growth, rendering a coarser texture (Figure S2c,f). Consequently, the active sites and electrochemical activity diminished (Figure S4). Among the various samples, the $NiCo_2S_4$@Mo-doped Co-LDH (reaction time = 3 h) showcased a desirable morphology and boasts the highest specific capacitance, rendering it ideal for asymmetric supercapacitors. The microstructure of the specimen was further scrutinized using transmission electron microscopy (TEM). The sample was delicately detached from the carbon cloth substrate. Consistent with the SEM findings, the $NiCo_2S_4$ nanowires were enveloped by Mo-doped Co-LDH nanosheets, resulting in captivating core-shell heterostructures (Figure 1h,i). The lattice D-spacing of 0.27 nm ascribed to (100) crystal plane of α-$Co(OH)_2$; this composition will be discussed in the XRD investigations.

X-ray diffraction (XRD) was conducted to scrutinize the intricate lattice arrangement and unravel the mystique of the crystal structures of $NiCo_2S_4$@Co-MOF and $NiCo_2S_4$@Mo-doped Co-LDH. Figure S3 exhibits the XRD patterns of NiCo-precursor and $NiCo_2S_4$. The diffraction peaks located at 9.9°, 17.5°, 19.9°, 24.1°, 26.7°, 28.7°, 30.4°, 33.8°, 35.4°, 36.5°, 39.5°, 44.6°, 47.3°, 54.1°, 56.1°, 59.8°, and 62.2° are well indexed with the (020), (001), (111), (220), (121), (300), (221), (040), (301), (231), (050), (340), (060), (142), (412), and (450) planes of $Ni_{2/3}Co_{4/3}(CO_3)(OH)_2$, respectively [33]. For the $NiCo_2S_4$ nanowires, the diffraction peaks located at 2θ values of 31.6°, 38.3°, 50.5°, and 55.3° could be identified as the (311), (400), (511), and (440) crystal planes (JCPDS No. 20-0782), respectively. As shown in Figure 2a (black line), following the mesmerizing blossoming of the MOF, a symphony of peaks gracefully emerged within the 10–40° range, harmoniously aligning with the resplendent XRD patterns of ZIF-67 [34,35]. The $NiCo_2S_4$ nanowires depict diffraction peaks at 16.3°, 27.1°, 31.6°, 38.3°, 50.5°, 55.2° (marked with circle), which were well correlated with (111), (220), (311), (400), (511), and (440) planes, respectively, clearly showing the cubic spinel crystal of $NiCo_2S_4$ (JCPDS No. 20-0782) [36,37]. The ethereal presence of graphitized carbon gracefully emanated from the carbon cloth, casting a spellbinding allure. This is demonstrated by the broad peaks at around 25°, corresponding to the (002) crystal planes.

As for the XRD pattern of $NiCo_2S_4$@Mo-doped Co-LDH (red line of Figure 2a), apart from those $NiCo_2S_4$ planes, peaks at 11.4°, 23.7°, 33.3°, 34.8°, 46.7°, and 59.1° (marked with rhombus) could be ascribed to (003), (006), (100), (102), (108), and (110) planes of α-$Co(OH)_2$ (JCPDS No. 46-0605) [38,39]. However, no obvious diffraction peaks related to Mo-based compound present in the XRD pattern of $NiCo_2S_4$@Mo-doped Co-LDH, meaning that the essence of Mo did not orchestrate the birth of a new crystalline realm during the enchanting MOF etching process. Instead, it gracefully infused itself into the very fabric of the MOF-derived Co-LDH, creating a harmonious fusion of elements [40,41].

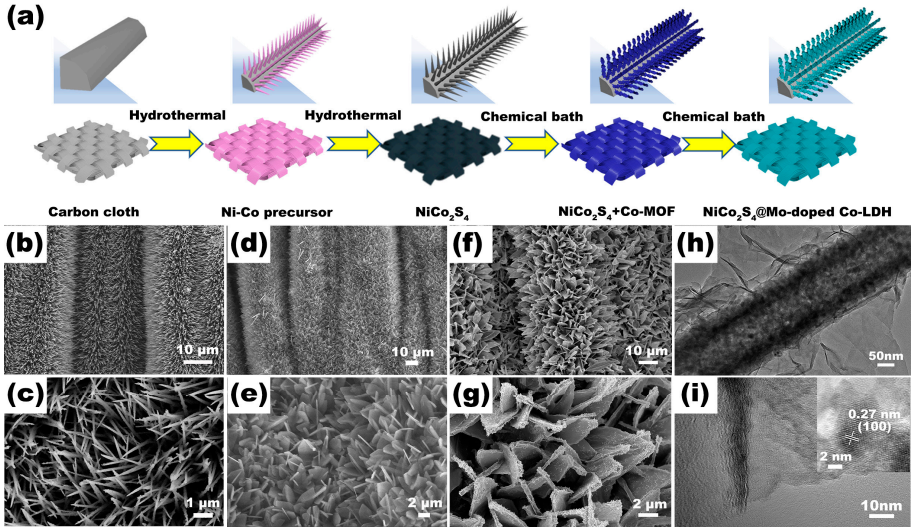

Figure 1. (**a**) Synthesis process of the $NiCo_2S_4$@Mo-doped Co-LDH. Low- and high-resolution SEM images of the (**b**,**c**) $NiCo_2S_4$, (**d**,**e**) $NiCo_2S_4$@Co-MOF, (**f**,**g**) $NiCo_2S_4$@Mo-doped Co-LDH. (**h**,**i**) Low- and high-resolution TEM images of the $NiCo_2S_4$@Mo-doped Co-LDH.

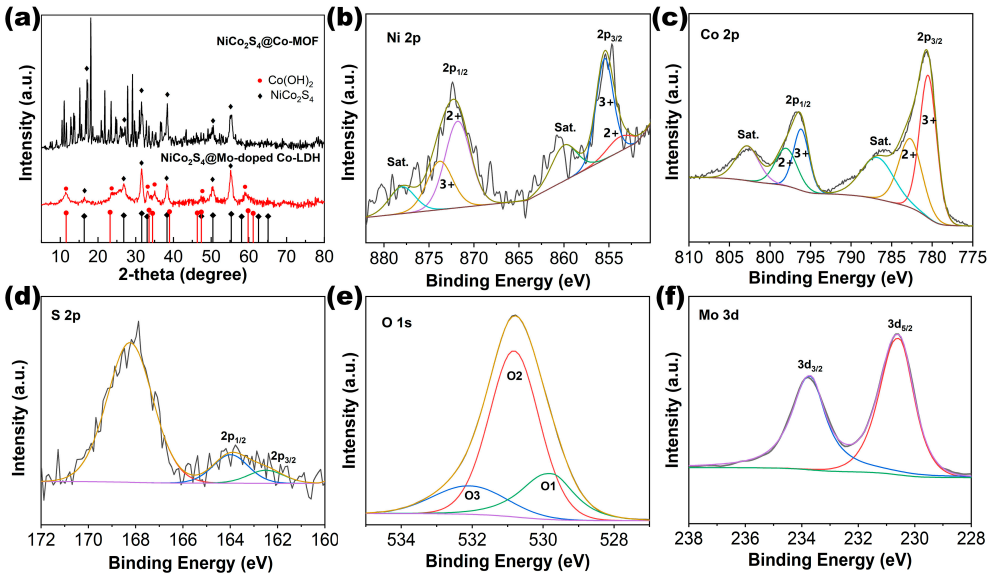

Figure 2. (**a**) XRD patterns of the $NiCo_2S_4$@Co-MOF and the $NiCo_2S_4$@Mo-doped Co-LDH. XPS spectra of the $NiCo_2S_4$@Mo-doped Co-LDH in the (**b**) Ni 2p, (**c**) Co 2p, (**d**) S 2p, (**e**) O 1s, and (**f**) Mo 3d regions.

The captivating elemental composition and chemical valence states of the $NiCo_2S_4$@Mo-doped Co-LDH were investigated using X-ray photoelectron spectroscopy (XPS). The survey spectrum, depicted in Figure S5, revealed the presence of Ni, Co, S, C, Mo, and O elements. Within the Ni 2p spectrum (Figure 2b), a fascinating narrative unfolded, as

evidenced by the binding energies of Ni $2p_{3/2}$ and Ni $2p_{1/2}$ at 855.1 and 872.9 eV, respectively, indicating the Ni^{2+} valence state. Additionally, the binding energies at 856.3 and 874.1 eV suggested the presence of the Ni^{3+} valence state [42]. Figure 2c unveils a captivating portrayal of the Co 2p spectrum, wherein two distinct peaks emerge with binding energies of 796.3.7 eV and 781.7 eV. These peaks elegantly signify the presence of Co^{3+} species. Another pair of characteristic peaks manifests at binding energies of 792.2 eV and 782.7 eV, distinctly representing Co^{2+}. The remarkable disparity of over 15 eV between the binding energies of these doublets elegantly confirms the coexistence of both Co^{2+} and Co^{3+} states. [43,44]. Figure 2d showcases the XPS spectrum of S 2p, revealing two spin-orbit peaks and an accompanying satellite peak. The peak located at 162.5 eV and 163.8 eV can be attributed to S $2p_{3/2}$ and S $2p_{1/2}$, while the satellite peak is accredited to surface adsorbed SO_3^{2-}/SO_4^{2-} species [32,45]. The O 1s XPS spectrum of $NiCo_2S_4$@Mo-doped Co-LDH, illustrated in Figure 2e, showcases a series of peaks associated with the metal–oxygen bond (M-OH), surface-bound OH groups, and chemisorbed water molecules [46]. Furthermore, the Mo 3d spectrum in Figure 2f exhibits two well-defined peaks at 234.0 eV and 231.7 eV, corresponding to Mo $3d_{3/2}$ and Mo $3d_{5/2}$, respectively, which can be accurately deconvoluted [47,48]. These peaks unequivocally signify the presence of Mo^{6+} species within the Mo-doped Co-LDH structure. Notably, compared to that of MoO_3, the Mo 3d spectrum of Mo-doped Co-LDH exhibits a negative shift over 1.0 eV, infesting an augmented electron density on the Mo^{6+} ions resulting from electron abstraction from the Co center [48,49]. This electron transfer leads to an increment in the charge on the Co atom, hence facilitating the redox reaction on the Mo-doped Co-LDH surface.

3.2. Electrochemical Measurements of the $NiCo_2S_4$@Mo-Doped Co-LDH

The electrochemical characteristics of $NiCo_2S_4$ and $NiCo_2S_4$@Mo-doped Co-LDH were assessed using cyclic voltammetry (CV), galvanostatic charge–discharge (GCD) measurements, and electrochemical impedance spectroscopy (EIS) in a three-electrode setup. Figure 3a compares CV plots of the $NiCo_2S_4$ and $NiCo_2S_4$@Mo-doped Co-LDH at 10 mV s^{-1} from −0.2 to 0.6 V. All CV diagrams possess obvious redox peaks, indicating the Faradaic reactions of the electrodes. As for the bare $NiCo_2S_4$, two prominent broad peaks (0.31 and 0.14 V) can be discerned, signifying the occurrence of a redox reaction involving the $Co^{2+/3+}$ and $Ni^{2+/3+}$ species [50,51]. With the integration of Mo-doped Co-LDH, two anodic peaks (0.02 and 0.28 V) and two cathodic peaks (−0.1 and 0.08 V) appeared, meaning that a more active redox reaction occurs on the composite structure. All the CV curves of these electrodes possess quasi-rectangular profiles, which can be ascribed to the faradaic reaction combined with surface capacitive nature. Moreover, the $NiCo_2S_4$@Mo-doped Co-LDH electrode apparently delivers a larger integral area and peak current than $NiCo_2S_4$, exhibiting an enhanced capacitive performance, the $NiCo_2S_4$@Mo-doped Co-LDH electrode demonstrates a synergistic effect between the two active materials. The cyclic voltammetry (CV) curves of the $NiCo_2S_4$@Mo-doped Co-LDH electrode, presented in Figure 3b, were obtained by varying the scan rates (5–50 mV s^{-1}) within a potential window of −0.2 to 0.6 V. It is worth mentioning that the current response demonstrates a direct relationship with the scan rate. Additionally, the anodic and cathodic peaks exhibit a notable shift towards more positive and negative potentials, respectively. Remarkably, the overall shape of the curves remains largely unchanged, indicating the exceptional electrochemical reversibility and high-rate capability of the core-shell $NiCo_2S_4$@Mo-doped Co-LDH electrode.

To investigate the charge storage mechanism of the $NiCo_2S_4$@Mo-doped Co-LDH electrode, the CV curves at different scan rates were analyzed by plotting log peak current vs. log scan rates according to power law ($i = av^b$) (Figure S6a), where i is the peak current of CV curves (A), v is scan rates (mV s^{-1}), and a and b refer to empirical parameters. When b value is close to 0.5, it implies the dominating diffusion controlled faradic process; meanwhile, a b value near 1 indicates capacitive controlled process. The b values of the $NiCo_2S_4$@Mo-doped Co-LDH electrode are 0.75 and 0.71, implying the co-existence of diffusion and capacitive controlled reversible process [52]. Moreover, to study the

charge storage contribution mechanisms of the $NiCo_2S_4$@Mo-doped Co-LDH electrode, the capacitive (K_1v) and diffusion ($K_2v^{1/2}$) contribution can be quantified according to the following equation: $i = K_1v + K_2v^{1/2}$, where i and v are the current response and scan rates, respectively (Figure S6b). The contribution histogram (Figure S6c) shows that the charge storage mechanism of the $NiCo_2S_4$@Mo-doped Co-LDH is governed by diffusion-controlled reaction at lower scan rates (69% at 5 mV s^{-1}). With the intercalation of ions at higher scan rates, the capacitive contribution increases gradually.

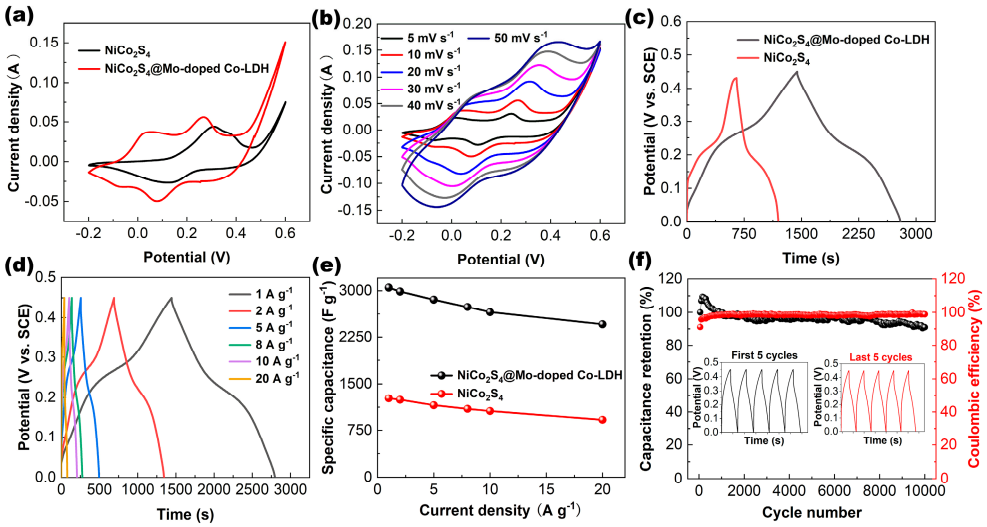

Figure 3. (**a**) CV and (**c**) GCD curves for the $NiCo_2S_4$ and the $NiCo_2S_4$@Mo-doped Co-LDH electrodes recorded at a scan rate of 10 mV s^{-1} and a current density of 1 A g^{-1}. (**b**) CV and (**d**) GCD curves of the $NiCo_2S_4$@Mo-doped Co-LDH electrode at various scan rate and current densities. (**e**) Specific capacitance of the $NiCo_2S_4$ and the $NiCo_2S_4$@Mo-doped Co-LDH electrodes at different current densities. (**f**) Cycling performances of the $NiCo_2S_4$@Mo-doped Co-LDH electrode at a current density of 10 A g^{-1}.

To evaluate the capacitive performance of both the $NiCo_2S_4$ and $NiCo_2S_4$@Mo-doped Co-LDH electrodes, galvanostatic charge–discharge (GCD) measurements were performed within a potential range of 0 to 0.45 V at 1 A g^{-1} (Figure 3c). Both electrodes exhibit distinct potential plateaus and symmetrical shapes, indicating their pseudocapacitive nature, which aligns well with the cyclic voltammetry (CV) results. Notably, the $NiCo_2S_4$@Mo-doped Co-LDH electrode demonstrates an extended discharge time compared to the pristine $NiCo_2S_4$ electrode, implying a significantly higher specific capacitance. Figure 3d presents representative GCD plots of the $NiCo_2S_4$@Mo-doped Co-LDH electrode tested from 1 to 20 A g^{-1}, within the potential window of 0 to 0.45 V. The maintained shape of the GCD curves, even at a high current density of 20 A g^{-1}, highlights the excellent rate performance, consistent with the CV findings. To achieve a comprehensive understanding of the charge storage mechanism of the electrodes, electrochemical impedance spectroscopy (EIS) measurements were performed (Figure S7). The equivalent circuit diagram (inset of Figure S7) consists of four major components, solution resistance (R_s), charge transfer resistance (R_{ct}), double-layer capacitive (CPE), and Warburg impedance (W) [28]. The Nyquist plots exhibit distinct intercepts where the semicircle intersects the Z′ axis in the high-frequency region, signifying the total internal resistance. Moreover, the sloped line observed in the low-frequency region corresponds to the semi-diffusion process occurring within the electrode materials [53]. Importantly, the EIS curve slope for the $NiCo_2S_4$@Mo-doped Co-LDH electrode is found to be greater than that of the $NiCo_2S_4$ electrode, which suggests enhanced ion diffusion and efficient electron transport within the composite structure.

In Figure 3e, the specific capacitance of the $NiCo_2S_4$@Mo-doped Co-LDH electrode was calculated to be 3049.3, 2986.9, 2857.5, 2741.2, 2654.8, and 2458.8 F g^{-1} at 1, 2, 5, 8, 10, and 20 A g^{-1}, respectively. These values significantly exceed those of the bare $NiCo_2S_4$ elec-

trode. Remarkably, even with a rapid increase from 1 to 20 A g^{-1}, the $NiCo_2S_4$@Mo-doped Co-LDH electrode maintains 80.6% of its initial specific capacitance, demonstrating its exceptional rate capability. Therefore, this material holds great promise for the fabrication of high-energy-density asymmetric supercapacitors. To assess the cycling performance of the $NiCo_2S_4$@Mo-doped Co-LDH electrode, the relationship between capacitance retention and cycle number is presented in Figure 3f. Following an activation process during the initial stage, the specific capacitance exhibits remarkable cycling stability, with a capacitance retention of 90.1% after 10,000 cycles, accompanied by a coulombic efficiency of approximately 100%. In contrast, under the same conditions, the $NiCo_2S_4$ electrode experiences a decrease to 71.7% (Figure S8), highlighting the beneficial effects of integrating Mo-doped Co-LDH on the structural and electrochemical stability of the core-shell architecture.

3.3. Electrochemical Measurements of the $NiCo_2S_4$@Mo-Doped Co-LDH//AC Asymmetric Supercapacitor

To evaluate the practical applicability of the synthesized $NiCo_2S_4$@Mo-doped Co-LDH electrode, a flexible all-solid-state asymmetric supercapacitor (ASC) was constructed. The mass ratio of the two electrodes was adjusted to ensure charge balance. The cyclic voltammetry (CV) curves of the activated carbon in the voltage range of −1 to −0.2 V exhibited a rectangular shape, indicating typical electric double-layer capacitance (EDLC) characteristics (Figure 4a). In contrast, the CV curve of the $NiCo_2S_4$@Mo-doped Co-LDH in the voltage range of −0.2 to 0.6 V displayed clear redox peaks, suggesting its pseudocapacitive behavior. This combination of materials effectively extended the voltage window of the device to 1.6 V. Figure S9 demonstrated the CV curves of the ASC device at various potential windows, revealing a gradual broadening of the curves as the potential range increased from 1.0 to 1.6 V. This confirmed the attainment of a 1.6 V potential window. Under this voltage window, Figure 4b illustrated the CV plots of the ASC at different scan rates. As the scan rate increased, the CV curves exhibited a combination of faradaic pseudocapacitive and EDLC characteristics, indicating favorable rate capability and a rapid current-voltage response. The triangular galvanostatic charge–discharge (GCD) plot in Figure 4c, obtained at various current densities, further validated the excellent capacitive behavior of the device. Electrochemical impedance spectroscopy (EIS) measurements (Figure S10) were employed to assess the electrochemical performance. The resulting plot displayed a semicircular shape at high frequencies and a linear shape at low frequencies, indicating outstanding capacitive behavior.

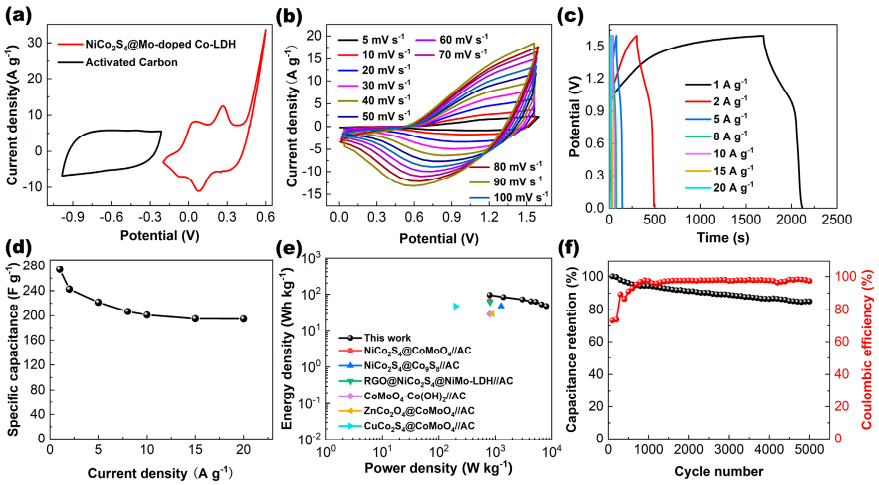

Figure 4. (**a**) CV curves of the AC and the $NiCo_2S_4$@Mo-doped Co-LDH electrodes. (**b**) CV and (**c**) GCD curves of the $NiCo_2S_4$@Mo-doped Co-LDH//AC ASC at various scan rate and current densities. (**d**) Rate capability of the ASC device. (**e**) Ragone plot of the ASC device. (**f**) Cycling stability of the supercapacitor device at 10 A g^{-1}.

The specific capacitance of the ASC reaches 274.2 F g^{-1} at 1 A g^{-1}, and even at a high current density of 20 A g^{-1}, the specific capacitance remains at 194.7 F g^{-1}, showcasing a remarkable rate capability of 71.1%. This demonstrates the superior capacitive behavior of the $NiCo_2S_4$@Mo-doped Co-LDH//AC ASC device (Figure 4d). The Ragone plot (Figure 4e) shows the relationship between energy density and power density in $NiCo_2S_4$@Mo-doped Co-LDH//AC ASC devices. At a power density of 835.6 W kg^{-1}, the ASC device achieves an ultra-high energy density of 97.5 Wh kg^{-1}. Even at a high power density of 23,511.7 W kg^{-1}, it maintains a maximum energy density of 69.2 Wh kg^{-1}.The obtained values are superior to several previously developed core-shell-structure-based ASC devices, including $NiCo_2S_4$@$CoMoO_4$//AC (66.6 Wh kg^{-1} at 800 W kg^{-1}) [54], $NiCo_2S_4$@Co_9S_8//AC (47.7 Wh kg^{-1} at 1275 W kg^{-1}) [55], RGO@$NiCo_2S_4$@NiMo-LDH//AC (61.0 Wh kg^{-1} at 808 W kg^{-1}) [56], $CoMoO_4$-$Co(OH)_2$//AC (29.2 Wh kg^{-1} at 800 W kg^{-1}) [53], $ZnCo_2O_4$@-oMoO_4//AC (29.3 Wh kg^{-1} at 884 W kg^{-1}) [57], and $CuCo_2S_4$@$CoMoO_4$//AC (47.5 Wh kg^{-1} at 199 W kg^{-1}) [58]. A comprehensive comparison of $NiCo_2S_4$@Mo-doped Co-LDH with other materials as an asymmetric supercapacitor is presented in Table S1. The charge–discharge cyclic stability under a current density of 10 A g^{-1} is depicted in Figure 4f. After 5000 cycles, the device exhibits a desirable cyclic stability of 85.0%, demonstrating its excellent durability for practical applications.

4. Conclusions

In summary, the hierarchical core-shell structure of the $NiCo_2S_4$@Mo-doped Co-LDH electrode, derived from MOF using a step-wise hydrothermal/solvent-thermal method, enhances overall conductivity and facilitates faster ion transport and electron conduction. Integration of MOF-derived Mo-doped Co-LDH further enhances the electrode's specific capacitance, exhibiting a remarkable value of 3049.3 F g^{-1} at 1 A g^{-1}. Additionally, the $NiCo_2S_4$@Mo-doped Co-LDH electrode demonstrates exceptional cyclic stability with 90.1% retention after 10,000 cycles at 10 A g^{-1}. The all-solid-state supercapacitor based on this electrode achieves an ultra-high energy density of 97.5 Wh kg^{-1} at a power density of 835.6 W kg^{-1}. The rational construction of the hierarchical core-shell structure using MOF as template significantly enhances the electrochemical performance; this characteristic renders it a highly promising contender for the development of future energy storage devices.

Supplementary Materials: The following supporting information can be downloaded at: https://www.mdpi.com/article/10.3390/nano13192663/s1, Figure S1: Low- and high-resolution SEM images of the NiCo-precursor; Figure S2: SEM of the $NiCo_2S_4$@Mo-doped Co-LDH at different synthesis times; Figure S3: XRD patterns of the NiCo-precursor and $NiCo_2S_4$; Figure S4: Comparison of GCD (a) and EIS (b) results of the $NiCo_2S_4$@Mo-doped Co-LDH at different synthesis times; Figure S5: Survey XPS spectra of the $NiCo_2S4$@Mo-doped Co-LDH; Figure S6: (a) Linear variation of log peak current and log scan rates. (b) Linear relation of i/v vs. v. (c) Diffusion contribution and capacitive contribution at various scan rates; Figure S7: EIS results of the $NiCo_2S_4$ and $NiCo_2S_4$@Mo-doped Co-LDH; Figure S8: Cycling performance of the $NiCo_2S_4$ electrode at 10 A g^{-1}; Figure S9: CV curves of the $NiCo_2S_4$@Mo-doped Co-LDH//AC ASC at various voltage window; Figure S10: EIS curve of the $NiCo_2S_4$@Mo-doped Co-LDH//AC ASC device; Table S1: Comparison of $NiCo_2S_4$@Mo-doped Co-LDH with other materials. Refs. [59–63] are cited in Supplementary Materials.

Author Contributions: S.C., Methodology, Software, Validation, Conceptualization, Writing—review and editing, and Visualization. K.D., Methodology, Software, Validation, and Resources. X.W., Conceptualization and Methodology. Y.H., Software, Validation, and Resources. L.L., Methodology, Validation, and Resources. G.W., Conceptualization, Funding acquisition, and Writing—reviewing and editing. All authors have read and agreed to the published version of the manuscript.

Funding: This research was funded by the National Natural Science Foundation of China under grant Nos. 52205611 and 41972325, the Natural Science Foundation of Hubei Province (2022CFB121), the Natural Science Foundation of Chongqing (CSTB2023NSCQ-MSX0941), and the Key Research and Development Project of Hubei Province (2020BAB054).

Data Availability Statement: The data presented in this study are available in the article and can be shared upon request.

Acknowledgments: The authors wish to express their gratitude for the financial support from the Engineering Research Center of Rock-Soil Drilling & Excavation and Protection, Ministry of Education.

Conflicts of Interest: The authors declare no conflict of interest.

References

1. Xing, F.; Bi, Z.; Su, F.; Liu, F.; Wu, Z.S. Unraveling the Design Principles of Battery-Supercapacitor Hybrid Devices: From Fundamental Mechanisms to Microstructure Engineering and Challenging Perspectives. *Adv. Energy Mater.* **2022**, *12*, 2200594. [CrossRef]
2. Kumar, S.; Saeed, G.; Zhu, L.; Hui, K.N.; Kim, N.H.; Lee, J.H. 0D to 3D carbon-based networks combined with pseudocapacitive electrode material for high energy density supercapacitor: A review. *Chem. Eng. J.* **2021**, *403*, 126352. [CrossRef]
3. Patil, S.A.; Rabani, I.; Hussain, S.; Seo, Y.-S.; Jung, J.; Shrestha, N.K.; Im, H.; Kim, H. A facile Design of Solution-Phase Based VS2 multifunctional electrode for green energy harvesting and storage. *Nanomaterials* **2022**, *12*, 339. [CrossRef] [PubMed]
4. Sekhar, S.C.; Ramulu, B.; Arbaz, S.J.; Hussain, S.K.; Yu, J.S. One-Pot Hydrothermal-Derived NiS_2–$CoMo_2S_4$ with Vertically Aligned Nanorods as a Binder-Free Electrode for Coin-Cell-Type Hybrid Supercapacitor. *Small Methods* **2021**, *5*, 2100335. [CrossRef] [PubMed]
5. Kothandam, G.; Singh, G.; Guan, X.; Lee, J.M.; Ramadass, K.; Joseph, S.; Benzigar, M.; Karakoti, A.; Yi, J.; Kumar, P. Recent Advances in Carbon-Based Electrodes for Energy Storage and Conversion. *Adv. Sci.* **2023**, *10*, 2301045. [CrossRef] [PubMed]
6. Zhao, J.; Wang, Y.; Qian, Y.; Jin, H.; Tang, X.; Huang, Z.; Lou, J.; Zhang, Q.; Lei, Y.; Wang, S. Hierarchical design of cross-linked NiCo2S4 nanowires bridged NiCo-hydrocarbonate polyhedrons for high-performance asymmetric supercapacitor. *Adv. Funct. Mater.* **2023**, *33*, 2210238. [CrossRef]
7. Yi, T.-F.; Pan, J.-J.; Wei, T.-T.; Li, Y.; Cao, G. $NiCo_2S_4$-based nanocomposites for energy storage in supercapacitors and batteries. *Nano Today* **2020**, *33*, 100894. [CrossRef]
8. Sharma, P.; Kumar, V. Current technology of supercapacitors: A review. *J. Electron. Mater.* **2020**, *49*, 3520–3532. [CrossRef]
9. Brousse, T.; Bélanger, D.; Long, J.W. To be or not to be pseudocapacitive? *J. Electrochem. Soc.* **2015**, *162*, A5185. [CrossRef]
10. Gogotsi, Y.; Penner, R.M. Energy storage in nanomaterials—Capacitive, pseudocapacitive, or battery-like? *ACS Nano* **2018**, *12*, 2081–2083. [CrossRef]
11. Park, H.W.; Roh, K.C. Recent advances in and perspectives on pseudocapacitive materials for supercapacitors—A review. *J. Power Sources* **2023**, *557*, 232558. [CrossRef]
12. Ho, K.-C.; Lin, L.-Y. A review of electrode materials based on core–shell nanostructures for electrochemical supercapacitors. *J. Mater. Chem. A* **2019**, *7*, 3516–3530. [CrossRef]
13. Yang, Q.; Lu, Z.; Li, T.; Sun, X.; Liu, J. Hierarchical construction of core–shell metal oxide nanoarrays with ultrahigh areal capacitance. *Nano Energy* **2014**, *7*, 170–178. [CrossRef]
14. Gonçalves, J.M.; da Silva, M.I.; Toma, H.E.; Angnes, L.; Martins, P.R.; Araki, K. Trimetallic oxides/hydroxides as hybrid supercapacitor electrode materials: A review. *J. Mater. Chem. A* **2020**, *8*, 10534–10570. [CrossRef]
15. Benadji, S.; Eloy, P.; Leonard, A.; Su, B.L.; Rabia, C.; Gaigneaux, E.M. Characterization of H_3+ $xPMo_{12}-xVxO_{40}$ heteropolyacids supported on HMS mesoporous molecular sieve and their catalytic performance in propene oxidation. *Microporous Mesoporous Mater.* **2012**, *154*, 153–163. [CrossRef]
16. Liu, J.; Wang, J.; Zhang, B.; Ruan, Y.; Lv, L.; Ji, X.; Xu, K.; Miao, L.; Jiang, J. Hierarchical $NiCo_2S_4$@NiFe LDH heterostructures supported on nickel foam for enhanced overall-water-splitting activity. *ACS Appl. Mater. Interfaces* **2017**, *9*, 15364–15372. [CrossRef] [PubMed]
17. Zhu, Y.; An, S.; Sun, X.; Lan, D.; Cui, J.; Zhang, Y.; He, W. Core-branched $NiCo_2S_4$@ CoNi-LDH heterostructure as advanced electrode with superior energy storage performance. *Chem. Eng. J.* **2020**, *383*, 123206. [CrossRef]
18. Huang, J.; Xie, J.; Wang, L.; Zhang, J.; Wang, P.; Sun, P.; Yao, Z.; Yang, Y. Boosted Electrochemical Performance of Honeycomb-Like NiCu–LDH Nanosheets Anchoring on NiCo2S4 Nanotube Arrays for Flexible Solid-State Hybrid Supercapacitors. *Energy Fuels* **2020**, *34*, 13157–13166. [CrossRef]
19. Singh, A.; Ojha, S.K.; Singh, M.; Ojha, A.K. Controlled synthesis of $NiCo_2S_4$@$NiCo_2O_4$ core@ Shell nanostructured arrays decorated over the rGO sheets for high-performance asymmetric supercapacitor. *Electrochim. Acta* **2020**, *349*, 136349. [CrossRef]
20. Liu, J.; Yang, Z.; Yang, L.; Zhu, Y.; Xue, T.; Xu, G. Rational design of yolk-shell $NiCo_2O_4$@ void@$NiCo_2S_4$ nanospheres for effective enhancement in microwave absorption. *J. Alloys Compd.* **2021**, *853*, 157403. [CrossRef]
21. Cheng, S.; Shi, T.; Huang, Y.; Tao, X.; Li, J.; Cheng, C.; Liao, G.; Tang, Z. Rational design of nickel cobalt sulfide/oxide core-shell nanocolumn arrays for high-performance flexible all-solid-state asymmetric supercapacitors. *Ceram. Int.* **2017**, *43*, 2155–2164. [CrossRef]
22. Huang, Y.; Shi, T.; Jiang, S.; Cheng, S.; Tao, X.; Zhong, Y.; Liao, G.; Tang, Z. Enhanced cycling stability of $NiCo_2S_4$@NiO core-shell nanowire arrays for all-solid-state asymmetric supercapacitors. *Sci. Rep.* **2016**, *6*, 38620. [CrossRef] [PubMed]
23. Liao, F.; Yang, G.; Cheng, Q.; Mao, L.; Zhao, X.; Chen, L. Rational design and facile synthesis of Ni-Co-Fe ternary LDH porous sheets for high-performance aqueous asymmetric supercapacitor. *Electrochim. Acta* **2022**, *428*, 140939. [CrossRef]

24. Cheng, Y.; Wang, X.; Zhang, D.; Qiao, X.; Zhao, H.; Chang, L.; Yu, Z.; Xia, Y.; Fan, J.; Huang, C. High-capacity binderless supercapacitor electrode obtained from sulfidation large interlayer spacing of NiMn-LDH. *Electrochim. Acta* **2022**, *429*, 141039. [CrossRef]
25. Zhang, R.; Dong, J.; Zhang, W.; Ma, L.; Jiang, Z.; Wang, J.; Huang, Y. Synergistically coupling of 3D FeNi-LDH arrays with Ti3C2Tx-MXene nanosheets toward superior symmetric supercapacitor. *Nano Energy* **2022**, *91*, 106633. [CrossRef]
26. Wang, X.; Huang, F.; Rong, F.; He, P.; Que, R. Unique MOF-derived hierarchical MnO_2 nanotubes@ NiCo-LDH/CoS_2 nanocage materials as high performance supercapacitors. *J. Mater. Chem. A* **2019**, *7*, 12018–12028. [CrossRef]
27. Poudel, M.B.; Lohani, P.C.; Acharya, D.; Kandel, D.R.; Kim, A.A.; Yoo, D.J. MOF derived hierarchical ZnNiCo-LDH on vapor solid phase grown CuxO nanowire array as high energy density asymmetric supercapacitors. *J. Energy Storage* **2023**, *72*, 108220. [CrossRef]
28. Poudel, M.B.; Kim, A.R.; Ramakrishan, S.; Logeshwaran, N.; Ramasamy, S.K.; Kim, H.J.; Yoo, D.J. Integrating the essence of metal organic framework-derived ZnCoTe–N–C/MoS_2 cathode and ZnCo-NPS-N-CNT as anode for high-energy density hybrid supercapacitors. *Compos. Part B Eng.* **2022**, *247*, 110339. [CrossRef]
29. Patil, S.A.; Katkar, P.K.; Kaseem, M.; Nazir, G.; Lee, S.-W.; Patil, H.; Kim, H.; Magotra, V.K.; Thi, H.B.; Im, H. Cu@ Fe-Redox Capacitive-Based Metal–Organic Framework Film for a High-Performance Supercapacitor Electrode. *Nanomaterials* **2023**, *13*, 1587. [CrossRef]
30. Rinawati, M.; Wang, Y.-X.; Chen, K.-Y.; Yeh, M.-H. Designing a spontaneously deriving NiFe-LDH from bimetallic MOF-74 as an electrocatalyst for oxygen evolution reaction in alkaline solution. *Chem. Eng. J.* **2021**, *423*, 130204. [CrossRef]
31. Tang, J.; Shen, Y.; Miao, X.; Qin, H.; Song, D.; Li, Y.; Qu, Y.; Yin, Z.; Ren, J.; Wang, L. Template-directed growth of hierarchically structured MOF-derived LDH cage hybrid arrays for supercapacitor electrode. *J. Electroanal. Chem.* **2019**, *840*, 174–181. [CrossRef]
32. Poudel, M.B.; Kim, A.A.; Lohani, P.C.; Yoo, D.J.; Kim, H.J. Assembling zinc cobalt hydroxide/ternary sulfides heterostructure and iron oxide nanorods on three-dimensional hollow porous carbon nanofiber as high energy density hybrid supercapacitor. *J. Energy Storage* **2023**, *60*, 106713. [CrossRef]
33. Wan, H.; Jiang, J.; Yu, J.; Xu, K.; Miao, L.; Zhang, L.; Chen, H.; Ruan, Y. $NiCo_2S_4$ porous nanotubes synthesis via sacrificial templates: High-performance electrode materials of supercapacitors. *CrystEngComm* **2013**, *15*, 7649–7651. [CrossRef]
34. Zhi, G.; Wang, W.; Zhou, Y.; Feng, L. ZIF-67-derived CoP/NC effectively supported Pt nanoparticles for methanol oxidation reaction. *Nanoscale* **2023**, *15*, 2948–2953. [CrossRef] [PubMed]
35. Chen, T.-Y.; Kuo, T.-R.; Yougbaré, S.; Lin, L.-Y.; Xiao, C.-Y. Novel direct growth of ZIF-67 derived Co_3O_4 and N-doped carbon composites on carbon cloth as supercapacitor electrodes. *J. Colloid Interface Sci.* **2022**, *608*, 493–503. [CrossRef] [PubMed]
36. Sun, Y.Y.; Zhang, X.Y.; Tang, J.; Li, X.; Fu, H.Q.; Xu, H.G.; Mao, F.; Liu, P.; Yang, H.G. Amorphous Oxysulfide Reconstructed from Spinel $NiCo_2S_4$ for Efficient Water Oxidation. *Small* **2023**, *19*, 2207965. [CrossRef] [PubMed]
37. Shen, X.; Li, H.; Zhang, Y.; Ma, T.; Li, Q.; Jiao, Q.; Zhao, Y.; Li, H.; Feng, C. Construction dual-regulated $NiCo_2S_4$@ Mo-doped CoFe-LDH for oxygen evolution reaction at large current density. *Appl. Catal. B Environ.* **2022**, *319*, 121917. [CrossRef]
38. Ranganatha, S.; Munichandraiah, N. Sol–gel synthesis of mesoporous α-$Co(OH)_2$ and its electrochemical performance evaluation. *ACS Omega* **2018**, *3*, 7955–7961. [CrossRef]
39. Cui, H.; Ma, W.; Wang, L.; Xue, J. Preparation of α-$Co(OH)_2$ monolayer nanosheets by an intercalation agent-free exfoliation process. *J. Sol-Gel Sci. Technol.* **2016**, *78*, 293–298. [CrossRef]
40. Guan, C.; Xiao, W.; Wu, H.; Liu, X.; Zang, W.; Zhang, H.; Ding, J.; Feng, Y.P.; Pennycook, S.J.; Wang, J. Hollow Mo-doped CoP nanoarrays for efficient overall water splitting. *Nano Energy* **2018**, *48*, 73–80. [CrossRef]
41. Xiao, Y.; Chen, X.; Li, T.; Mao, Y.; Liu, C.; Chen, Y.; Wang, W. Mo-doped cobalt hydroxide nanosheets coupled with cobalt phosphide nanoarrays as bifunctional catalyst for efficient and high-stability overall water splitting. *Int. J. Hydrogen Energy* **2022**, *47*, 9915–9924. [CrossRef]
42. Lin, J.; Zhong, Z.; Wang, H.; Zheng, X.; Wang, Y.; Qi, J.; Cao, J.; Fei, W.; Huang, Y.; Feng, J. Rational constructing free-standing Se doped nickel-cobalt sulfides nanotubes as battery-type electrode for high-performance supercapattery. *J. Power Sources* **2018**, *407*, 6–13. [CrossRef]
43. Lv, Y.; Duan, S.; Zhu, Y.; Yin, P.; Wang, R. Enhanced OER performances of Au@$NiCo_2S_4$ core-shell heterostructure. *Nanomaterials* **2020**, *10*, 611. [CrossRef] [PubMed]
44. Li, X.; Yin, S.; Cai, L.; Wang, Z.; Zeng, C.; Jiang, H.; Cheng, J.; Lu, W. Sea-urchin-like $NiCo_2S_4$ modified MXene hybrids with enhanced microwave absorption performance. *Chem. Eng. J.* **2023**, *454*, 140127. [CrossRef]
45. Li, X.-X.; Wang, X.-T.; Xiao, K.; Ouyang, T.; Li, N.; Liu, Z.-Q. In situ formation of consubstantial $NiCo_2S_4$ nanorod arrays toward self-standing electrode for high activity supercapacitors and overall water splitting. *J. Power Sources* **2018**, *402*, 116–123. [CrossRef]
46. Singh, B.; Indra, A. Tuning the properties of CoFe-layered double hydroxide by vanadium substitution for improved water splitting activity. *Dalton Trans.* **2021**, *50*, 2359–2363. [CrossRef] [PubMed]
47. Bao, J.; Wang, Z.; Xie, J.; Xu, L.; Lei, F.; Guan, M.; Huang, Y.; Zhao, Y.; Xia, J.; Li, H. The CoMo-LDH ultrathin nanosheet as a highly active and bifunctional electrocatalyst for overall water splitting. *Inorg. Chem. Front.* **2018**, *5*, 2964–2970. [CrossRef]
48. Zeng, N.; Hopkinson, D.G.; Spencer, B.F.; McAdams, S.G.; Tedstone, A.A.; Haigh, S.J.; Lewis, D.J. Direct synthesis of MoS_2 or MoO_3 via thermolysis of a dialkyl dithiocarbamato molybdenum (iv) complex. *Chem. Commun.* **2019**, *55*, 99–102. [CrossRef]
49. Singh, B.; Patel, A.K.; Indra, A. Introduction of high valent Mo6+ in Prussian blue analog derived Co-layered double hydroxide nanosheets for improved water splitting. *Mater. Today Chem.* **2022**, *25*, 100930. [CrossRef]

50. Wan, H.; Liu, J.; Ruan, Y.; Lv, L.; Peng, L.; Ji, X.; Miao, L.; Jiang, J. Hierarchical configuration of $NiCo_2S_4$ nanotube@ Ni–Mn layered double hydroxide arrays/three-dimensional graphene sponge as electrode materials for high-capacitance supercapacitors. *ACS Appl. Mater. Interfaces* **2015**, *7*, 15840–15847. [CrossRef]
51. Sui, Y.; Zhang, Y.; Hou, P.; Qi, J.; Wei, F.; He, Y.; Meng, Q.; Sun, Z. Three-dimensional $NiCo_2S_4$ nanosheets as high-performance electrodes materials for supercapacitors. *J. Mater. Sci.* **2017**, *52*, 7100–7109. [CrossRef]
52. Poudel, M.B.; Kim, H.J. Confinement of Zn-Mg-Al-layered double hydroxide and α-Fe_2O_3 nanorods on hollow porous carbon nanofibers: A free-standing electrode for solid-state symmetric supercapacitors. *Chem. Eng. J.* **2022**, *429*, 132345. [CrossRef]
53. Zhao, Y.; Dong, H.; He, X.; Yu, J.; Chen, R.; Liu, Q.; Liu, J.; Zhang, H.; Yu, J.; Wang, J. Carbon Cloth Modified with Metal-Organic Framework Derived CC@ $CoMoO_4$-$Co(OH)_2$ Nanosheets Array as a Flexible Energy-Storage Material. *ChemElectroChem* **2019**, *6*, 3355–3366. [CrossRef]
54. Zhao, Y.; He, X.; Chen, R.; Liu, Q.; Liu, J.; Song, D.; Zhang, H.; Dong, H.; Li, R.; Zhang, M. Hierarchical $NiCo_2S_4$@$CoMoO_4$ core-shell heterostructures nanowire arrays as advanced electrodes for flexible all-solid-state asymmetric supercapacitors. *Appl. Surf. Sci.* **2018**, *453*, 73–82. [CrossRef]
55. Han, X.; Chen, Q.; Zhang, H.; Ni, Y.; Zhang, L. Template synthesis of $NiCo_2S_4$/Co_9S_8 hollow spheres for high-performance asymmetric supercapacitors. *Chem. Eng. J.* **2019**, *368*, 513–524. [CrossRef]
56. Cheng, C.; Zou, Y.; Xu, F.; Xiang, C.; Sui, Q.; Zhang, J.; Sun, L.; Chen, Z. Ultrathin graphene@ $NiCo_2S_4$@Ni-Mo layered double hydroxide with a 3D hierarchical flowers structure as a high performance positive electrode for hybrid supercapacitor. *J. Energy Storage* **2022**, *52*, 105049. [CrossRef]
57. Yu, D.; Teng, Y.; Liu, X.; Liu, X. A high-performance electrode based on the $ZnCo_2O_4$@$CoMoO_4$ core-shell nanosheet arrays on nickel foam and their application in battery-supercapacitor hybrid device. *Electrochim. Acta* **2020**, *347*, 136278.
58. Mao, X.; Wang, Y.; Xiang, C.; Zhan, D.; Zhang, H.; Yan, E.; Xu, F.; Hu, X.; Zhang, J.; Sun, L.; et al. Core-shell structured $CuCo_2S_4$@$CoMoO_4$ nanorods for advanced electrode materials. *J. Alloys Compd.* **2020**, *844*, 156133. [CrossRef]
59. Jia, H.; Wang, J.; Fu, W.; Hu, J.; Liu, Y. In-situ MOFs-derived hollow Co_9S_8 polyhedron welding on the top of $MnCo_2S_4$ nanoneedles for high performance hybrid supercapacitors. *Chem. Eng. J.* **2020**, *391*, 123541. [CrossRef]
60. Sui, Y.; Zhang, Y.; Hu, H.; Xu, Q.; Yang, F.; Li, Z. High energy density asymmetric supercapacitor based ZnS/$NiCo_2S_4$/Co_9S_8 nanotube composites materials. *Adv. Mater. Interfaces* **2018**, *5*, 1800018. [CrossRef]
61. Zhang, Y.; Xu, J.; Zheng, Y.; Zhang, Y.; Hu, X.; Xu, T. $NiCo_2S_4$@$NiMoO_4$ core-shell heterostructure nanotube arrays grown on Ni foam as a binder-free electrode displayed high electrochemical performance with high capacity. *Nanoscale Res. Lett.* **2017**, *12*, 412. [CrossRef]
62. Guo, Y.; Hao, C.; Wang, X.; Yang, Y.; Wang, X.; Wu, J.; Shen, Y. Facile fabrication of CoNi-Layered Double Hydroxide/$NiCo_2S_4$/Reduced Graphene Oxide composites by in situ hydrothermal growth strategy for supercapacitor performance. *Ceram. Int.* **2022**, *48*, 17644–17653. [CrossRef]
63. Tang, Y.; Liu, X.; Chen, Y.; Han, L.; Dai, D.; Liu, L.; Wang, C.; Hua, Y.; Zhao, X.; Liu, X. $NiCo_2S_4$@MoS_2 core/shell nanorod arrays for fabrication of high-performance asymmetric supercapacitors with high mass loading. *J. Energy Storage* **2022**, *51*, 104518. [CrossRef]

Disclaimer/Publisher's Note: The statements, opinions and data contained in all publications are solely those of the individual author(s) and contributor(s) and not of MDPI and/or the editor(s). MDPI and/or the editor(s) disclaim responsibility for any injury to people or property resulting from any ideas, methods, instructions or products referred to in the content.